Available online at www.sciencedirect.com
ScienceDirect
International Journal of Refrigeration 30 (2007) 1347–1357
REVUE INTERNATIONALE DU FROID
INTERNATIONAL JOURNAL OF
refrigeration
www.elsevier.com/locate/ijrefrig

Comparison of parallel- and counter-flow circuiting in an industrial evaporator under frosting conditions

N.F. Aljuwayhel, D.T. Reindl*, S.A. Klein, G.F. Nellis

University of Wisconsin – Madison, 1500 Engineering Drive, Madison, WI 53706, USA

Received 10 July 2006; received in revised form 10 February 2007; accepted 9 April 2007
Available online 27 April 2007

Abstract

This paper describes a theoretical model of a large-scale, ammonia-fed evaporator coil used in an industrial refrigeration system and operating under low temperature air and refrigerant conditions that are typically encountered in refrigerated storage spaces. The model is used to simulate the performance of counter-flow and parallel-flow circuited evaporator coil designs under frosting conditions. The counter-flow frost model is validated using in situ data obtained from a field-installed evaporator coil. The performance of an evaporator in a parallel-flow circuit arrangement is simulated and compared to counter-flow circuiting. The effects of coil circuiting are evaluated in terms of the frost distribution across the evaporator coil and the associated reduction in cooling capacity during operation.

Keywords: Cooling; Evaporator; Finned tube; Industrial application; Ammonia; R-717; Modelling; Heat transfer; Parallel flow; Counter-flow; Frost formation

Comparaison de l'écoulement parallèle et à contre-courant dans un évaporateur industriel sous des conditions de givrage

Mots clés : Réfrigération ; Évaporateur ; Tube aileté ; Application industrielle ; Ammoniac ; R-717 ; Modélisation ; Transfert de chaleur ; Écoulement parallèle ; Écoulement croisé ; Givrage

1. Introduction

Frost will accumulate on the surfaces of evaporator coils that operate at temperatures below 0 °C when the entering air dew point temperature is above the coil temperature. Frost accumulation is a serious problem that leads to a reduction in both the capacity and the efficiency of a refrigeration system. The degradation in performance is related to the low conductivity of the frost layer which adds an additional thermal resistance between the air and the refrigerant and, more importantly, the reduction in air flow rate that is caused by the increased resistance to air flow through the narrowing channels due to the growing frost layer. The higher flow resistance reduces the amount of air that the evaporator fan can move through the coil.

* Corresponding author. Tel.: +1 608 262 6381.
E-mail address: dreindl@wisc.edu (D.T. Reindl).

0140-7007/$35.00 © 2007 Elsevier Ltd and IIR. All rights reserved.
doi:10.1016/j.ijrefrig.2007.04.009

Nomenclature

A_b	bare tube outside surface area (m^2)
A_{tot}	total heat transfer area (m^2)
A_e	effective heat transfer area (m^2)
A_{fin}	fin surface area (m^2)
$A_{fin,c}$	contact surface area between the coil tubes and the fins (m^2)
A_i	tube cross-section area (m^2)
cp_a	specific heat for air ($J\,kg^{-1}\,K^{-1}$)
D_i	tube inside diameter (m)
D_o	tube outside diameter (m)
F_{thk}	fin thickness (m)
h_a	convective air-side heat transfer coefficient ($W\,m^{-2}\,K^{-1}$)
h_m	mass transfer coefficient ($kg\,m^{-2}\,s^{-1}$)
h_{lat}	latent heat transfer coefficient ($W\,m^{-2}\,K^{-1}$)
h_{eff}	effective air heat transfer coefficient ($W\,m^{-2}\,K^{-1}$)
h_{tp}	two-phase refrigerant heat transfer coefficient ($W\,m^{-2}\,K^{-1}$)
i	enthalpy ($kJ\,kg^{-1}$)
I_n	modified Bessel function of the first kind (nth order)
k_{fin}	fin thermal conductivity ($W\,m^{-1}\,K^{-1}$)
k_f	frost thermal conductivity ($W\,m^{-1}\,K^{-1}$)
k_{tube}	tube thermal conductivity ($W\,m^{-1}\,K^{-1}$)
K_n	modified Bessel function of the second kind (nth order)
Le	Lewis number
m	fin constant (Eq. (12))
$\dot{m}$	mass flow rate ($kg\,s^{-1}$)
P_{fin}	fin pitch (m)
P_t	transverse tube pitch (m)
P_r	longitudinal tube pitch (m)
$\dot{q}_{tot}$	total heat transfer rate (W)
$\dot{q}_{lat}$	latent heat transfer rate (W)
$\dot{q}_{sen}$	sensible heat transfer rate (W)
R_c	thermal contact resistance ($m^2\,K\,W^{-1}$)
R_{fa}	air-side fouling factor ($m^2\,K\,W^{-1}$)
R_{fr}	refrigerant-side fouling factor ($m^2\,K\,W^{-1}$)
r_1	tube outside radius (m)
r_2	fin equivalent radius (m)
T	temperature (K)

Greek symbols

ρ	density ($kg\,m^{-3}$)
η_f	fin efficiency
η_{fc}	total fin efficiency
ω	specific humidity
δ_f	thickness of frost layer (m)

Subscripts

a	air
ave	averaged
f	frost
fa	fouling on air-side
fr	fouling on refrigerant-side
in	inlet to the evaporator coil section
lm	log-mean
out	outlet from the evaporator coil section
r	refrigerant
sg	sublimation change

The process of frost formation on the surfaces of an evaporator coil is a result of two mechanisms. The first mechanism is the buildup of small ice particles that exist in the free air stream and accumulate by impaction or interception when they contact the evaporator coil surfaces [1,2]. The air stream in this case is supersaturated; i.e., a metastable state that is initiated when moist warm air is suddenly cooled, causing the moisture in the air to transform into tiny ice crystals. These ice crystals normally appear as a dense "fog" and they have an affinity for cold surfaces. Because the frost associated with the accumulation of these ice particles has a low density, it can build up very rapidly. The blockage of air flow through the coil can be mitigated or managed by mechanical or pneumatic (air knife) removal. This type of frost formation process is observed in regions of very large moisture content, for example evaporator coils that are located near doors or in blast freezers that are freezing unpackaged products.

The second mechanism for frost growth is the diffusion of water vapor onto cold surfaces due to the difference in the water vapor concentration of the air stream and the surface of the frost layer [3]. The water mass that is transferred to the frost surface creates two distinct effects in the frost layer. A portion of the water vapor is deposited onto the frost layer; thereby, contributing to further frost growth while the remainder of the water vapor diffuses into the frost layer where it changes phase and densifies the frost. This type of frost layer forms relatively slowly with a very high density. Because of its dense structure, it is typically not possible to mechanically or pneumatically control or remove this type of frost; therefore, it must be periodically removed using a defrost process. The high density frost formation process is observed in regions of relatively low air temperature with low moisture content, for example evaporator coils that are placed in a refrigerated warehouse used for the long-term storage of food products.

Regardless of the frost formation mechanism, it is necessary to periodically remove the frost (i.e., defrost the coil) in order to maintain an acceptable level of evaporator thermal performance. Because all defrost processes require energy and result in a parasitic load on the refrigerated space, they must be properly managed to balance operational necessity

with the energy penalty associated with carrying out a defrost process. There is also a penalty associated with continuing to allow the buildup of frost which further deteriorates the performance of the evaporator. This tradeoff leads to an optimal time between successive defrosts based on a balance between these penalties. As a first step towards identifying the optimal defrost parameters, this paper presents a theoretical model that quantifies the reduction in the cooling capacity of an evaporator coil as frost accumulates on its surface.

Models for frost formation on finned-tube heat exchangers have been described in the literature [4–8]. However, these models were developed and validated using experimental data obtained from heat exchangers designed for applications other than industrial refrigeration, including domestic refrigeration systems, air source heat pumps and unitary HVAC systems.

This paper presents a theoretical model developed specifically for a large-scale, air-cooling evaporator coils typically used in industrial ammonia refrigeration systems operating under low air and refrigerant temperature conditions. The type of frost considered in this paper is a high density frost that accumulates relatively slowly. The model is used to simulate and compare the performance of evaporator coil designs with both counter-flow and parallel-flow circuiting. The counter-flow frost model is validated using in situ data obtained in the field from a counter-flow evaporator coil installed in a refrigerated warehouse used to store food products.

2. Formulation of the model

A liquid overfed evaporator coil consisting of multiple rows of finned tube with multiple refrigerant circuits (Fig. 1) is considered. The model is formulated for a single refrigerant circuit (Fig. 2) that is assumed to be representative of the remaining (n) circuits in the coil.

An individual evaporator circuit is divided into a number of sections that is equal to the total number of the coil rows

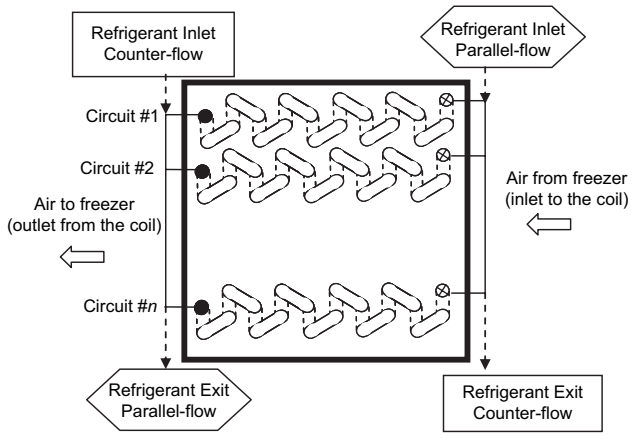

Fig. 1. Schematic diagram showing an evaporator coil with multiple rows of finned tubes with multiple refrigerant circuits and the direction of the air and the refrigerant flow for both the counter-flow and the parallel-flow arrangements.

in the flow direction (10 for the geometry shown in Fig. 2). The thermal properties of the freezer air are the inlet conditions associated with the first section. The outlet air and refrigerant properties for each section become the inlet properties for the next section (Fig. 3).

The evaporator coil air-side heat transfer surfaces are rectangular plate fins that are modeled as equivalent circular fins each attached to a tube (Fig. 4) according to Schmidt [9].

The evaporator has a cross-flow configuration in which the direction of the air flow is perpendicular to the direction of the refrigerant flow. Almost all industrial evaporator coils are designed so that the refrigerant enters from the back side of the evaporator coil (i.e., the air exit side) in what is referred to as a counter-flow arrangement, as shown in Fig. 1. However, the present model is formulated so that the refrigerant inlet can be reversed, allowing the refrigerant to enter from the front side of the evaporator coil (i.e., the air inlet side) in order to simulate a parallel-flow arrangement. This small change in circuiting has a significant impact in the performance of the evaporator under frosting conditions, as discussed in Section 4.

2.1. Heat and mass transfer equations

An energy balance relates the enthalpy reduction of the moist air stream to the increase in the enthalpy of the two-phase refrigerant within each section of the evaporator:

$$\dot{q}_{\mathrm{tot}} = \dot{m}_{\mathrm{a}}(i_{\mathrm{a,in}} - i_{\mathrm{a,out}}) = \dot{m}_{\mathrm{r}}(i_{\mathrm{r,out}} - i_{\mathrm{r,in}}) \tag{1}$$

where $\dot{m}_{\mathrm{a}}$ and $\dot{m}_{\mathrm{r}}$ are the air and refrigerant mass flow rates, respectively. Because the energy associated with the moisture leaving the air stream and being deposited on the coil surface is small compared with the energy change of the moist air across the coil, it is neglected from the air-side energy balance. The variables $i_{\mathrm{r,in}}$ and $i_{\mathrm{r,out}}$ represent the inlet and outlet refrigerant enthalpies, respectively. The variables $i_{\mathrm{a,in}}$ and $i_{\mathrm{a,out}}$ are the inlet and outlet air enthalpies, which are a function of the inlet and outlet air temperature, pressure and relative humidity.

The total heat transfer rate $(\dot{q}_{\mathrm{tot}})$ is the sum of the sensible heat transfer rate $(\dot{q}_{\mathrm{sen}})$, and the latent heat transfer rate $(\dot{q}_{\mathrm{lat}})$. The sensible heat transfer rate can be expressed as:

$$\dot{q}_{\mathrm{sen}} = h_{\mathrm{a}}A_{\mathrm{e}}\left(T_{\mathrm{a,ave}} - T_{\mathrm{f,ave}}\right) \tag{2}$$

where h_{a} is the air-side heat transfer coefficient, A_{e} is the effective heat transfer area associated with the section which is equal to the sum of the bare tubing surface area (A_{b}) and the fin surface area (A_{f}) reduced by the total fin efficiency (η_{fc}):

$$A_{\mathrm{e}} = A_{\mathrm{b}} + \eta_{\mathrm{f}}A_{\mathrm{fc}} \tag{3}$$

$T_{\mathrm{f,ave}}$ and $T_{\mathrm{a,ave}}$ are the average frost surface temperature and the average air dry bulb temperature within the section, respectively. The average air temperature is defined as:

$$T_{\mathrm{a,ave}} = T_{\mathrm{r,ave}} + \Delta T_{\mathrm{lm}} \tag{4}$$

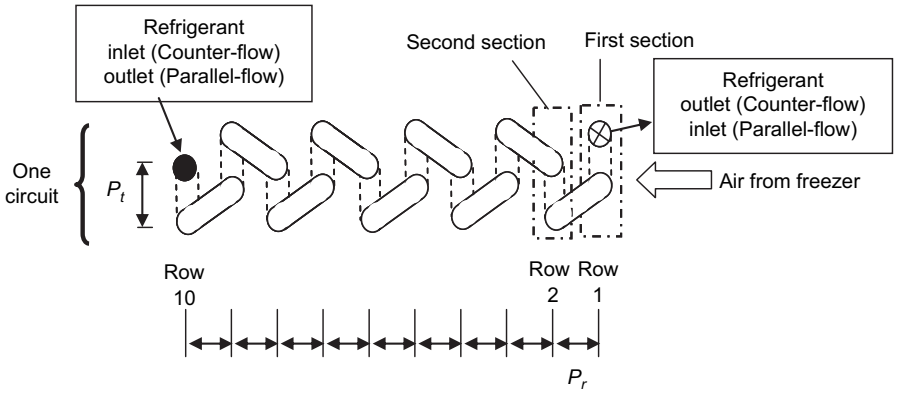

Fig. 2. Schematic diagram showing one evaporator coil circuit and the direction of the air and the refrigerant flow for both the counter-flow and the parallel-flow arrangements.

where $T_{r,ave}$ is the average refrigerant temperature and ΔT_{lm} is the log-mean temperature difference between the air and the refrigerant.

Because the typical air-cooling evaporator in an industrial refrigeration system is driven by a constant speed fan, the air mass (and volume) flow rate will decrease as frost accumulates and increases the flow resistance of the coil. As a consequence, the air-side convective heat transfer coefficient (h_a in Eq. (2)) will also change. In the model, the mass flow rate of air through the coil is determined by the intersection of the evaporator's fan curve and the resistance curve associated with the frosted coil. Specific correlations for the air-side pressure drop or convective heat transfer coefficient associated with a frosted coil were not found. Rather, the pressure drop equation described in Kays and London [10] is used with a friction factor correlation suggested by McQuiston [11]. A correlation suggested by McQuiston [11] is used to calculate the air-side convective heat transfer coefficient. These correlations were developed for a bare coil; however, the effect of the frost build up is approximately included by using the air mass flux based on the minimum free flow area and the local velocity considering the effect of the frost thickness.

The latent heat transfer rate is calculated using the convective mass transfer coefficient (h_m) defined by Threlkeld [12]:

$$h_m = \frac{h_a}{Le\, cp_a} \tag{5}$$

where Le is the Lewis number and cp_a is the specific heat capacity of dry air. According to Threlkeld, the Lewis number for water vapor in air lies in the range of 0.90–0.92. Other investigators have used slightly different values of the Lewis number in their calculations; for example, Domanski [13], McQuiston [14], and Malhammar [1] use a Lewis number of 1.0 while Oskarsson and Krakow [4] suggest a Lewis number of 0.95 and Al-mutawa [15] uses a Lewis number of 0.845. For the current study, a Lewis number of 1.0 is used and a sensitivity analysis showing the effect of Lewis number on the model predictions is presented in Section 5.

The latent heat transfer rate is calculated according to:

$$\dot{q}_{lat} = h_m i_{sg} A_e \left(\omega_{a,ave} - \omega_f\right) \tag{6}$$

where i_{sg} is the heat of sublimation of water, and $\omega_{a,ave}$ and ω_f are the average humidity ratio of the air and the saturation

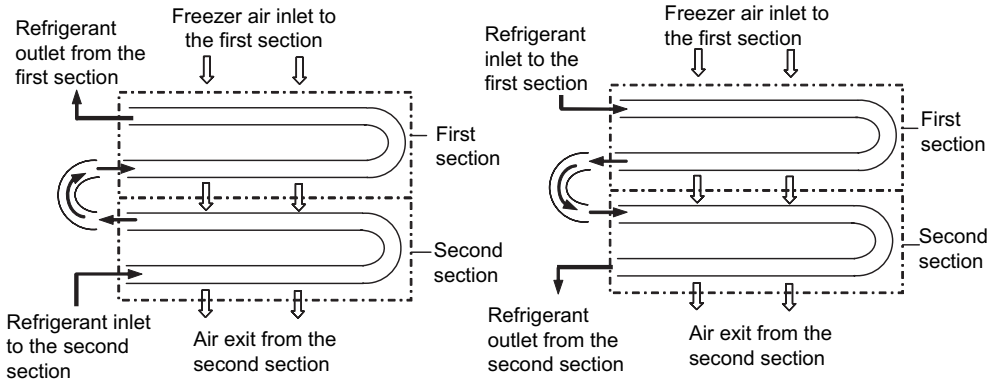

Fig. 3. Schematic of the first and the second evaporator coil sections as well as the direction of the air and the refrigerant flow for counter- (left) and, parallel- (right) flow arrangement.

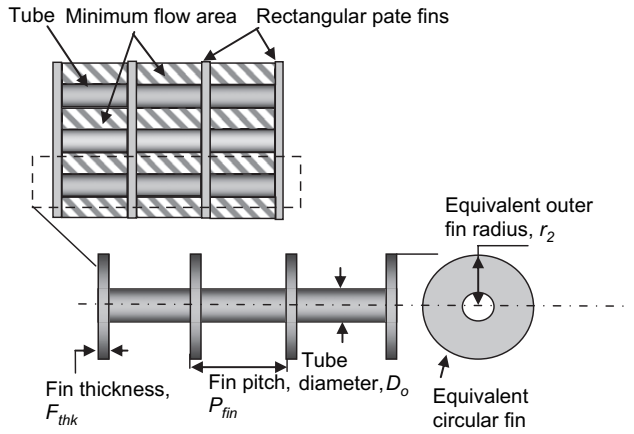

Fig. 4. Schematic of a heat exchanger showing the minimum flow area shaded with downward diagonal lines, fin pitch and fin thickness, and the equivalent circular fin.

humidity ratio at the frost surface temperature, respectively. The average specific humidity of the air is calculated as suggested by Oskarsson and Krakow [4]:

$$\frac{\omega_{a,ave}-\omega_{a,in}}{\omega_{a,out}-\omega_{a,in}}=\frac{T_{a,ave}-T_{a,in}}{T_{a,out}-T_{a,in}} \tag{7}$$

where $\omega_{a,in}$ and $\omega_{a,out}$ are the specific humidities of the entering and the exiting air at each evaporator section.

Rearranging Eq. (6) so that it has the same form as Eq. (2) yields:

$$\dot{q}_{lat}=h_{lat}A_e\left(T_a-T_f\right) \tag{8}$$

where h_{lat} is the latent heat transfer coefficient which can be expressed as:

$$h_{lat}=h_m i_{sg}\left(\frac{\omega_{a,ave}-\omega_f}{T_{a,ave}-T_f}\right) \tag{9}$$

The total heat transfer rate within any section of the heat exchanger is then:

$$\dot{q}_{tot}=\dot{q}_{sen}+\dot{q}_{lat}=(h_a+h_{lat})A_e\left(T_{a,ave}-T_f\right) \tag{10}$$

The fin efficiency (η_f) is calculated for a circular fin with an adiabatic tip according to Incropera and DeWitt [16]:

$$\eta_f=\frac{2r_1}{m(r_2^2-r_1^2)}\left[\frac{K_1(mr_1)I_1(mr_2)-K_1(mr_2)I_1(mr_1)}{I_0(mr_1)K_1(mr_2)+K_0(mr_1)I_1(mr_2)}\right] \tag{11}$$

where I_n and K_n are modified Bessel functions of the nth order (the first and second kinds), r_1 and r_2 are the inner and outer radii of the equivalent circular fin, respectively, and m is the fin constant given by:

$$m=\sqrt{\frac{2h_{eff}}{k_{fin}F_{thk}}} \tag{12}$$

where k_{fin} is the conductivity of the fin material, F_{thk} is the fin thickness and h_{eff} is the effective heat transfer coefficient. The effective heat transfer coefficient is defined so that it accounts for both latent and sensible heat transfer as well as for the conductive resistance of the frost layer:

$$h_{eff}=\left(\frac{1}{(h_a+h_{lat})}+\frac{\delta_f}{k_f}\right)^{-1} \tag{13}$$

where δ_f is the thickness of the frost layer and k_f is the average frost thermal conductivity which is calculated using the correlation developed by Lee et al. [17]. The inclusion of the latent heat transfer coefficient and the insulation effect of the frost in the fin efficiency, as described by Eqs. (12) and (13), were previously described by Kondepudi and O'Neal [6].

A thermal contact resistance between the coil tubes and the fins (R_c) is included in the total fin efficiency (η_{fc}) using Eq. (14):

$$\frac{1}{\eta_{fc}A_{fin}h_{eff}}=\frac{1}{\eta_f A_{fin}h_{eff}}+\frac{R_c}{A_{fin,c}} \tag{14}$$

where $A_{fin,c}$ is the contact surface area between the coil tubes and the fins. Rearranging Eq. (14) yields:

$$\eta_{fc}=\eta_f\left[1+\eta_f A_{fin}h_{eff}\left(\frac{R_c}{A_{fin,c}}\right)\right]^{-1} \tag{15}$$

The value of the assumed thermal contact resistance is:

$$R_c=0.0625\times10^{-4}\left(\mathrm{m^2\,K\,W^{-1}}\right) \tag{16}$$

The rate at which water vapor is transferred from the air stream to the coil surface $(\dot{m}_f)$ is calculated using a mass balance:

$$\dot{m}_f=\dot{m}_a(\omega_{a,in}-\omega_{a,out})=h_m A_e\left(\omega_{a,ave}-\omega_f\right) \tag{17}$$

The frost layer density (ρ_f) at any time is calculated using a system of equations developed by Malhammar [1]. The increase in the frost layer thickness $(\Delta\delta_f)$ over a specific time interval of duration (Δt) is calculated according to:

$$\Delta\delta_f=\frac{\dot{m}_f\Delta t}{A_{tot}\rho_f} \tag{18}$$

where (A_{tot}) is the total heat transfer area. Note that Eq. (18) implies that the frost will form uniformly over the tube and the fin surface at any location; however, the model allows for the non-uniform buildup of frost through successive rows in the coil.

The total heat transfer rate can finally be expressed as:

$$\dot{q}_{tot}=\frac{(T_{a,ave}-T_{r,ave})}{\frac{1}{(h_a+h_{lat})A_e}+\frac{\delta_f}{k_f A_e}+\frac{R_{fa}}{A_e}+\frac{\ln(D_o/D_i)}{2\pi Lk_{tube}}+\frac{1}{h_{tp}A_i}+\frac{R_{fr}}{A_i}} \tag{19}$$

where k_{tube} is the thermal conductivity of the tubes and h_{tp} is the refrigerant-side two-phase heat transfer coefficient computed using a system of equations developed by Jung and Didion [18]. R_{fa} and R_{fr} are the fouling factor on the air

and the refrigerant-side. The fouling factors as suggested by Rosenhow et al. [19] are:

$$R_{fa} = 3.5 \times 10^{-4} \left(m^2\,K\,W^{-1}\right) \quad (20)$$

$$R_{fr} = 3.5 \times 10^{-4} \left(m^2\,K\,W^{-1}\right) \quad (21)$$

Pressure drop on the refrigerant-side has typically been ignored in frost models (for example, [6,7]); however, the refrigerant-side pressure drop plays a significant role in the industrial evaporator coils because it may produce a non-negligible temperature change on the refrigerant-side of the circuit which can affect the distribution of the frost formation and therefore the behavior of the coil under frosting conditions. The frictional pressure drop on the refrigerant-side within the straight tube sections is calculated using correlations developed by Muller and Heck [20] and the inertial pressure drop associated with the flow of the two-phase refrigerant through the tube bends is calculated using correlations developed by Paliwoda [21].

3. Counter-flow frost model validation

The equations and correlations described in the previous section are combined to form the evaporator model for both counter-flow and parallel-flow circuiting. The predictions of the counter-flow frost model are compared with experimental data obtained from a field experiment on an industrial air-cooling evaporator; the details of this experiment and the resulting data are described by Aljuwayhel et al. [22]. The details associated with the experimental evaporator coil are summarized in Table 1.

Although the inlet air dry bulb temperature and relative humidity vary slightly throughout any experiment, constant values of −27.7 °C inlet air temperature and 90% inlet air relative humidity were used for the simulations since these values represent the averages observed during the experiment. The fan curve provided by the evaporator coil manufacturer was used to predict the variation in the air flow rate as the coil accumulates frost; thereby, imposing an air-side pressure drop. Liquid ammonia from a controlled-pressure receiver enters the evaporator with a temperature of −34.4 °C and quality of 7%.

Fig. 5 shows the time variation of the average air velocity at the evaporator coil face measured in the experiment (an average of measurements made at five spatial locations across the face taken for five different experimental runs) as well as the air velocity predicted by the counter-flow frost model (solid line). Both the experimental data and the frost model show that the air velocity decreases with time; this behavior is mainly due to the increase in the air flow resistance caused by the frost accumulation on the evaporator coil surfaces. Also, it can be seen from Fig. 5 that the air velocity predicted by the counter-flow frost model agrees reasonably well with the measured average air velocity. Details on the uncertainty analysis associated with the experiments are provided elsewhere (Aljuwayhel et al. [22]).

Table 1
Geometry and operating conditions of the coil used in the experiment

Parameter	Value
Fin pitch (cm)	0.85
Face area (m^2)	8.23
Tube diameter (m)	0.019
Tube length (m)	5.5
Number of tubes	260
Number of tube row	10
Tube transverse pitch (m)	0.057
Tube longitudinal pitch (m)	0.044
Coil mass (kg)	3900
Number of fans	5
Horse power per fan at 30 F (hp)	3.125
Rated CFM ($m^3\,min^{-1}$)	1.699
Evaporation temperature (°C)	−34.4
Coil temperature difference (°C)	5.5
Base rating ($kW\,K^{-1}$)	23.8
Nominal capacity (kW)	130
Fin/tube material	Aluminum/carbon steel
Refrigerant	Ammonia
Evaporator coil type	Controlled-pressure receiver-liquid overfeed

Fig. 6 compares the inlet to outlet air temperature difference measured during the experiment with the frost model prediction. Note that the measured temperature difference is the bulk temperature averaged over five spatially separated velocity and temperature measurements and that five separate experimental runs are shown. Fig. 6 shows that the temperature difference predicted by the counter-flow frost model matches the data to within experimental uncertainty over the entire frost process. Both the model prediction and the experimental data show that the inlet to outlet air temperature difference increases monotonically due to the reduction in the air flow rate. As the air flow rate drops, the coil effectiveness is increased and thus the exiting air

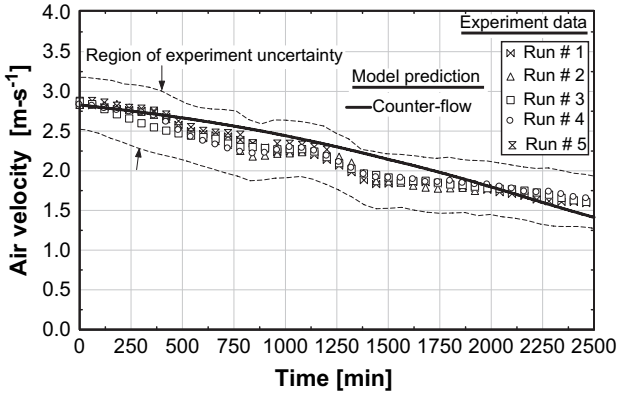

Fig. 5. Comparison between the average face velocity of the evaporator coil measured in the experiment and the face velocity predicted by the counter-flow frost model over time.

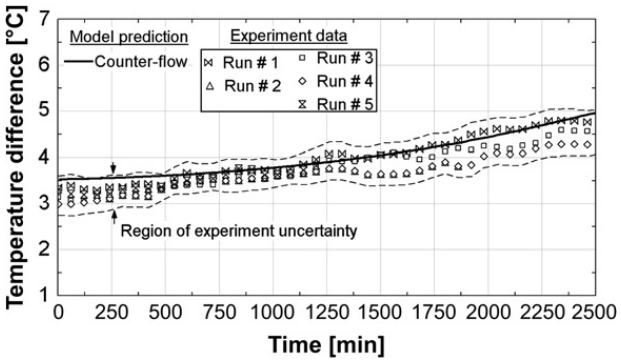

Fig. 6. Comparison of the inlet and outlet air temperature difference measured during the experiment and the temperature difference predicted by the counter-flow frost model over time.

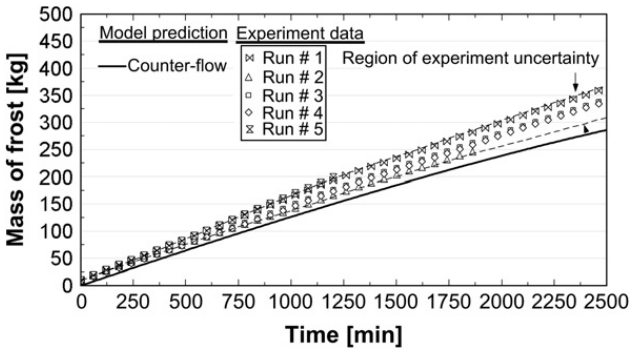

Fig. 8. Comparison of the total mass of frost predicted by the counter-flow frost model and the total mass of frost obtained using the experimental data over time.

temperature more closely approaches the refrigerant-side temperature.

Fig. 7 shows the evaporator cooling capacity obtained from an air-side energy balance using the experimental data and predicted by the counter-flow frost model. The evaporator coil cooling capacity decreases monotonically due to the increase in the air flow resistance as well as the insulating effect of the frost. The cooling capacity predicted by the counter-flow frost model agrees well with the measured evaporator cooling capacity.

Fig. 8 shows the total accumulated mass of frost based on a water vapor mass balance using the experimental data and predicted by the counter-flow frost model. The total mass of the accumulated frost increases nearly linearly with time and the counter-flow model slightly under-predicts the experimental data.

4. Counter-flow versus parallel-flow operation

Fig. 9 compares the evaporator cooling capacity predicted by the frost model using counter-flow and parallel-flow circuiting for otherwise the same evaporator geometry and operating conditions (Table 1).

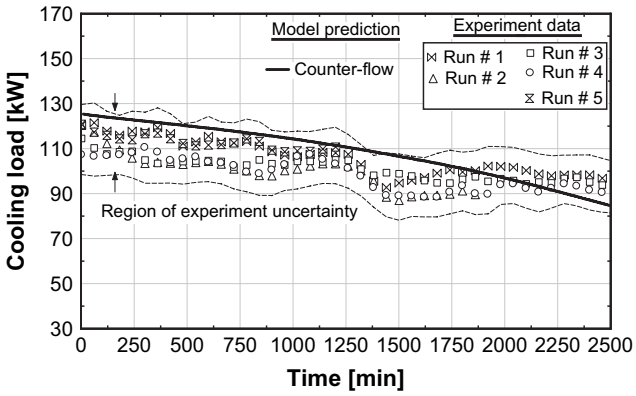

Fig. 7. Comparison of the evaporator cooling capacity measured during the experiment and the evaporator cooling capacity predicted by the counter-flow frost model over time.

Fig. 9 shows that there are several advantages associated with using the parallel-flow configuration as compared to the more conventional, counter-flow circuiting arrangement. The dry coil cooling capacity predicted for the parallel-flow circuiting (i.e., the capacity at the beginning of the simulation) is 8% higher than for the counter-flow arrangement; this observation agrees with the predictions of Nelson [23], who suggested that there is a 3–4% performance advantage associated with a parallel-flow circuiting arrangement for liquid ammonia overfed evaporator coils operating under dry conditions. The reason for the dry coil advantage is evident by observing the trends shown in Figs. 10 and 11.

Fig. 10 shows a row-by-row comparison of the refrigerant temperature, air temperature, and the overall heat transfer coefficient at the beginning of the simulation (time = 0) for the (a) parallel-flow and (b) counter-flow arrangements. Fig. 10a shows that the temperature difference between the ammonia and the air in a parallel-flow configuration decreases slightly for the coils that are deeper into the evaporator (i.e., coils with higher row numbers) whereas the overall heat transfer coefficient increases with row number.

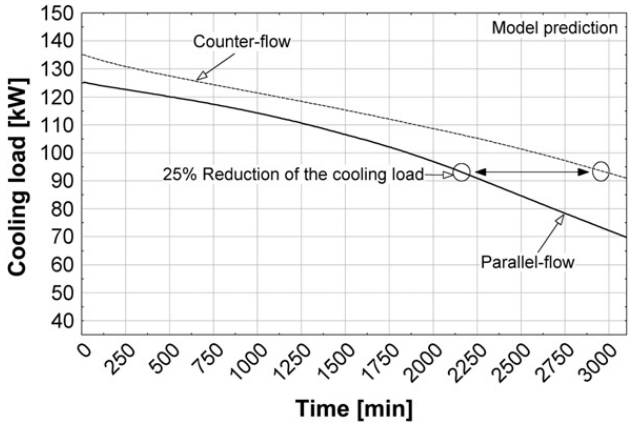

Fig. 9. Comparison between the evaporator cooling capacity predicted by the counter-flow frost model and the parallel-flow frost model versus time.

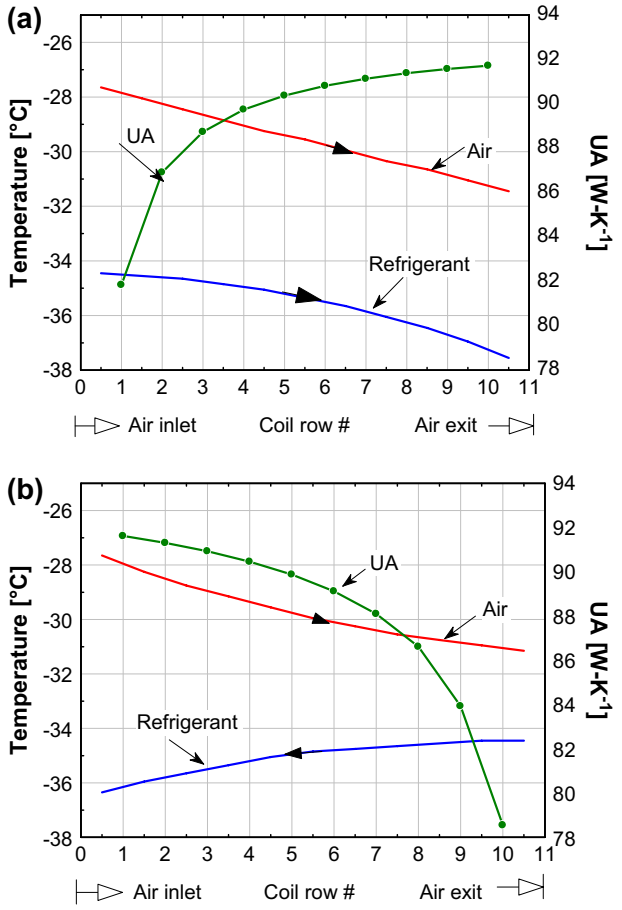

Fig. 10. Predicted air and refrigerant temperature and *UA* across the evaporator coil for the (a) parallel-flow and (b) counter-flow configurations.

These effects balance and result in a nearly uniform distribution of the cooling load, as shown in Fig. 11. The decrease in the refrigerant temperature is due to the decrease in refrigerant pressure associated with frictional and inertial pressure loss while the change in the overall heat transfer coefficient is due to the increase in the refrigerant quality as it evaporates. Fig. 10b shows that the temperature difference between the ammonia refrigerant and the air in a counter-flow configuration will decrease significantly with increasing coil rows as will the overall heat transfer coefficient. As a result, more of the cooling capacity will be provided by the first few coil rows, as shown in Fig. 11.

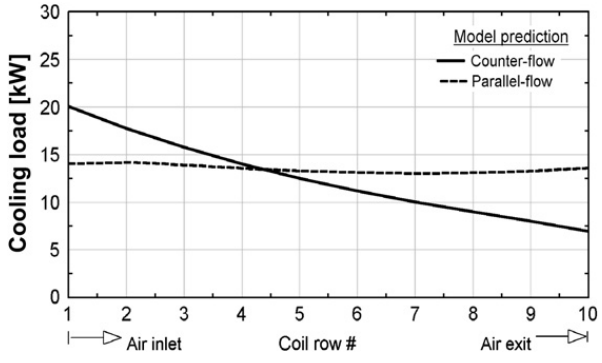

Fig. 11. Cooling capacity across the evaporator for the counter-flow and parallel-flow configurations.

Overall, the effectiveness of the counter-flow configuration is somewhat lower than the effectiveness of the parallel-flow configuration which results in a slight reduction in the initial cooling capacity of the coil. It is interesting that this trend towards higher effectiveness for a parallel-flow configuration is exactly opposite of what is expected for a conventional heat exchanger; this counter-intuitive result occurs because the temperature of the refrigerant (which is increasing in enthalpy) will actually decrease in the direction of flow because of refrigerant-side pressure drop.

Another and potentially more significant advantage of the parallel-flow over the counter-flow circuiting arrangement arises due to the manner in which frost accumulates on the coil surface. The effectiveness advantage of the parallel-flow configuration tends to increase with time as frost accumulates; this effect is shown in Fig. 9 where the predicted cooling capacity for the parallel-flow arrangement at the end of the simulation is 15% higher than the cooling capacity predicted by the counter-flow arrangement. The improvement in the cooling performance under frosting conditions is primarily due to the characteristics of the frost accumulation and the associated effect on the air-side pressure drop. Just as the first few rows of the counter-flow configuration tend to supply most of the refrigeration, these rows also tend to accumulate most of the frost. Therefore, after the same amount of operating time, the minimum air-side flow area (which tends to dominate the flow resistance of the coil) for the counter-flow configuration will be much less than for the parallel-flow configuration and the air-side flow resistance will be much higher. During operation, the counter-flow arranged coil will realize an equally diminished capacity 25% faster than the parallel-flow configured coil. Fig. 12 shows the calculated air velocity as a function of time and illustrates that the air flow reduction due to frost buildup is substantially higher for the counter-flow configuration even though the total mass of the accumulated frost is actually slightly smaller (see Fig. 13).

Fig. 14 illustrates the distribution of the rate of frost accumulation after 1 h of simulation for the parallel-flow and counter-flow configurations and shows that the frost accumulates more uniformly for the parallel-flow circuit. Fig. 15 shows the percent blockage as a function of time for selected rows in the coil for the (a) counter-flow and (b) parallel-flow configurations; the counter-flow arrangement results in almost a 45% difference in the percent blockage between the first and the last rows at the end of the simulation while there is only a 8.5% difference for the parallel-flow arrangement.

Fig. 15 shows that the first row of the counter-flow coil will reach 74% blockage at the end of the simulation as

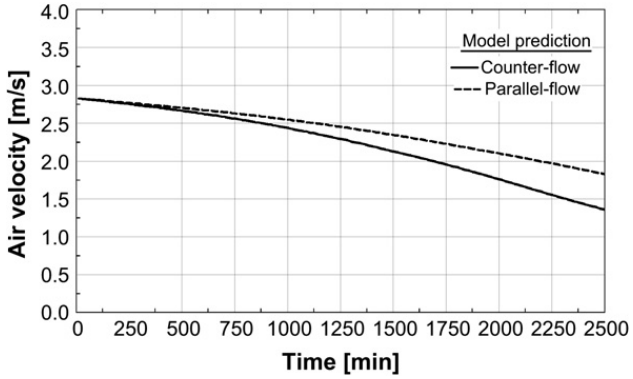

Fig. 12. Comparison between the air velocity predicted by the counter-flow frost model and the parallel-flow frost model over time.

compared to only 58% blockage for the last row of the parallel-flow arrangement. This result clearly shows that parallel-flow evaporator coils can operate for a longer time before they must be defrosted. If, for example, the defrost cycle is initiated when the evaporator cooling capacity drops by 25%, then with the parallel-flow arrangements, the cooling mode period can be extended in time by 38% (13.5 h), as shown in Fig. 9.

Finally comparing Figs. 14 and 16, it can be seen that although the frost accumulation rate for the parallel-flow arrangement decreases slightly for the deeper coils, the density of the accumulated frost, as predicted by the model, also slightly decreases. Therefore, the frost thickness is slightly larger at the last row than it is for the first row in the parallel-flow arrangement.

5. Effects of Lewis number on the frost model prediction

To assess the sensitivity of the counter-flow frost model to the value of the Lewis number, simulations were run using identical conditions but varying Lewis numbers between

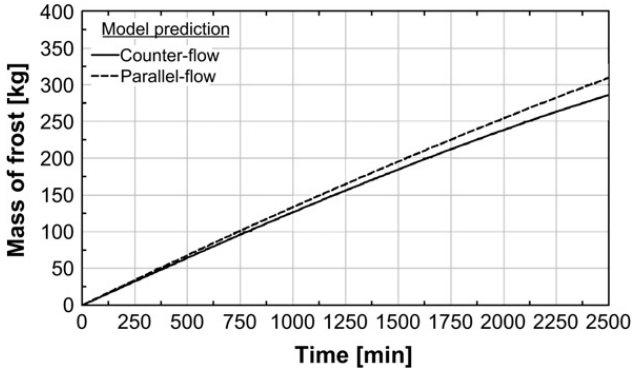

Fig. 13. Comparison between the total mass of the accumulated frost predicted by the counter-flow and the parallel-flow frost models over time.

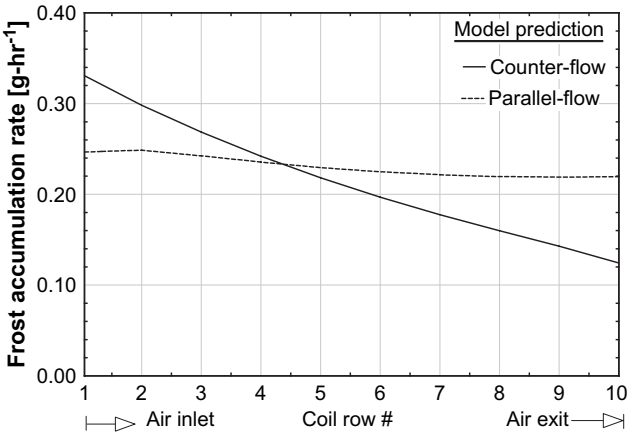

Fig. 14. Comparison of the frost accumulation rate at each row predicted by the counter-flow frost model and the parallel-flow frost model after 1h of operation.

0.85 and 1.0. The predicted frost accumulation, total mass of accumulated frost and the cooling capacity are compared in Figs. 16 and 17.

Fig. 16 shows that as the Lewis number decreases, the frost accumulation rate will increase. Eventually, the high rate of frost accumulation leads to larger mass of accumulated frost and as a consequence, a higher pressure drop and lower air velocity. Fig. 16 shows that at some point

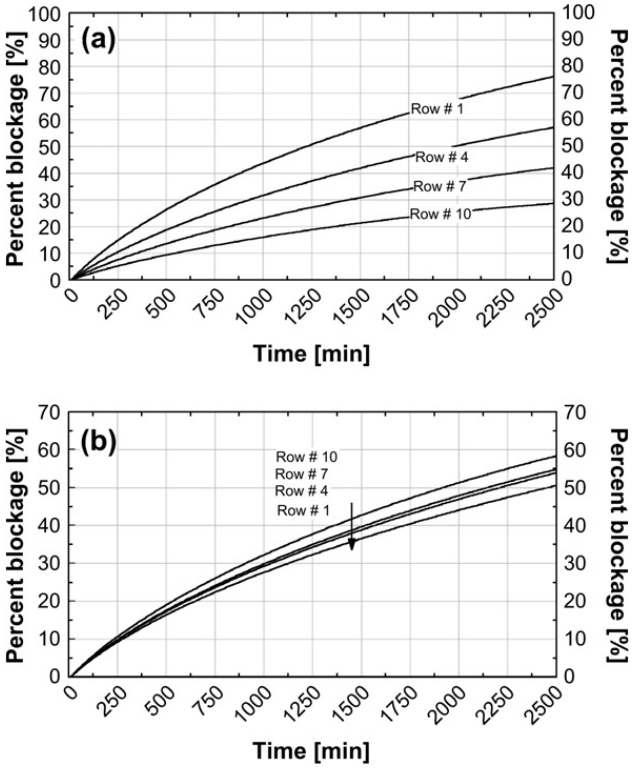

Fig. 15. Percent blockage of the air path caused by frost accumulation at different rows of the evaporator coil over time for (a) counter-flow and (b) parallel-flow circuiting.

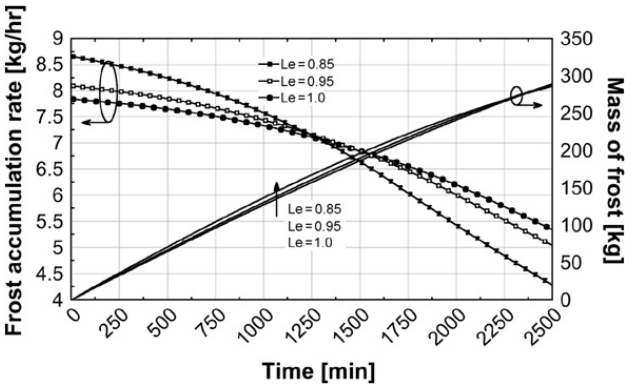

Fig. 16. Frost accumulation rate and the total mass for accumulated frost over time for three different Lewis numbers.

during the simulation, the frost accumulation rate predicted using a Lewis number of 0.85 will drop faster than for a Lewis number of 1.0. These effects balance and cause the total mass of the accumulated frost at the end of the simulation for Lewis numbers between 0.85 and 1.0 to be nearly the same. However the frost distribution across the evaporator coil is not the same. The accumulated frost is more concentrated in the first few rows for the smaller value of Lewis number and therefore the air velocity drops faster for the Lewis number of 0.85 as compared to 1.0. The cooling coil capacity prediction is therefore slightly higher for the larger Lewis number, as shown in Fig. 17.

6. Conclusion

A theoretical model of an evaporator coil subjected to frost accumulation has been developed and validated. The counter-flow evaporator model is validated using in situ data obtained from an air-cooling evaporator coil (counter-flow) installed in a refrigerated warehouse. The validated model is used to compare the performance of counter-flow and parallel-flow circuiting under frosting conditions. The impact of using parallel-flow as opposed to counter-flow circuiting is evaluated in terms of the frost distribution across the evaporator coil and the associated temporal reduction in cooling capacity during operation.

The current study shows there are two key advantages of the parallel-flow versus the counter-flow evaporator coils. First, the effectiveness of the counter-flow overfed industrial evaporator coils is slightly less than the effectiveness of the parallel-flow overfed industrial air-cooling evaporator coils and; therefore, the parallel-flow configuration provided slightly higher initial coil cooling capacity. Second, the cooling coil capacity advantage of the parallel-flow versus the counter-flow configuration tends to increase with time as frost accumulates, primarily due to the distribution of the accumulated frost and its effect on the air-side pressure drop. Therefore, parallel-flow evaporator coils can be used for a longer period of time before they must be defrosted.

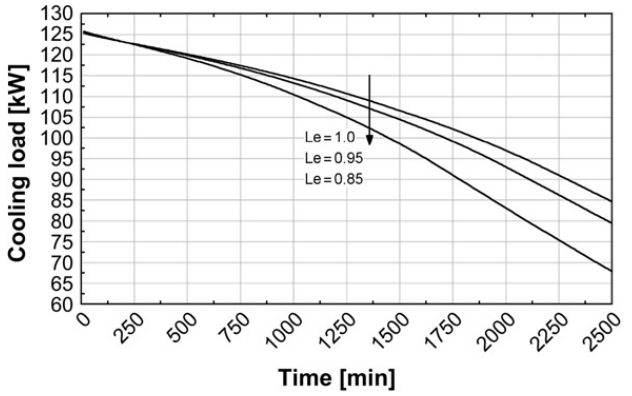

Fig. 17. Cooling coil capacity prediction of the counter-flow frost model for three different Lewis numbers.

References

[1] A. Malhammar, Monitoring frost growth in evaporators is a complex process, Australian Refrigeration, Air conditioning and Heat April (1988).
[2] P. Mango, S. Sherif, Psychrometric charts and property formulations of supersaturated air, HVAC&R Research 11 (1) (2005).
[3] C. Sanders, The Influence of Frost Formation and Defrosting on the Performance of Air Coolers, PhD dissertation, Delft University, The Netherlands, 1974.
[4] S. Oskarsson, K. Krakow, Evaporator models for operation with dry, wet and frosted finned surfaces – part I&II, ASHRAE Transactions 96 (1) (1990).
[5] S. Kondepudi, D. O'Neal, A simplified model of pin fin heat exchangers under frosting conditions, ASHRAE Transactions 99 (1) (1993).
[6] S. Kondepudi, D. O'Neal, Performance of finned-tube heat exchangers under frosting conditions: part I – simulation model, International Journal of Refrigeration 16 (3) (1993).
[7] D. Seker, H. Karatas, N. Egrican, Frost formation on fin-and-tube heat exchangers: part I&II, International Journal of Refrigeration 27 (4) (2004).
[8] Y. Yao, Y. Jiang, S. Deng, Z. Ma, A study on the performance of the airside heat exchanger under frosting in an air source heat pump water heater/chiller unit, International Journal of Heat and Mass Transfer 47 (2004).
[9] T. Schmidt, Heat transfer calculation for extended surfaces, Refrigerating Engineering 57 (1949).
[10] W. Kays, A. London, Compact Heat Exchangers, McGraw-Hill Book Company, New York, 1964.
[11] F. McQuiston, Finned tube heat exchangers: state of the art for the air-side, ASHRAE Transactions 87 (1) (1981).
[12] J. Threlkeld, Thermal Environmental Engineering, second ed., Prentice Hall Book Co., Englewood Cliffs, NJ, 1970.
[13] P. Domanski, Computer Modeling and Prediction of an Air Source Heat Pump with a Capillary Tube, PhD dissertation, The Catholic University of America, 1982.
[14] F. McQuiston, Fin efficiency with combined heat and mass transfer, ASHRAE Transactions 81 (1) (1975).

[15] N. Al-mutawa, Experimental Investigations of Frosting and Defrosting of Evaporator Coils at Freezer Temperature, PhD dissertation, The University of Florida, 1997.
[16] F. Incropera, D. DeWitt, Introduction to Heat Transfer, second ed., John Wiley & Sons, 1990.
[17] K. Lee, T. Lee, W. Kim, Heat and mass transfer of parallel heat exchanger under frosting conditions, SAREK Journal 6 (2) (1994).
[18] D. Jung, D. Didion, Horizontal Flow Boiling Heat Transfer Using Refrigerant Mixtures, Electric Power Research Institute, 1989, (ER-6364, EPRI Project 8006-2).
[19] W.M. Rosenhow, J.P. Hartnett, E.N. Ganic, Handbook of Heat Transfer Applications, second ed. McGraw Hill, New York, 1985.
[20] H. Muller, K. Heck, A simple friction pressure drop correlation for two-phase flow heat transfer of ammonia, Chemical Engineering Processing 20 (1986).
[21] A. Paliwoda, Generalized method of pressure drop calculation across pipe components containing two-phase flow of refrigerants, International Journal of Refrigeration 15 (2) (1992).
[22] N. Aljuwayhel, D. Reindl, S. Klein, G. Nellis, Experimental investigation of the performance of industrial evaporator coils operating under frosting conditions, International Journal of Refrigeration, in press, doi:10.1016/j.ijrefrig.2007.05.010.
[23] B. Nelson, Design of evaporators for liquid overfeed systems, ASHRAE Transactions 96 (1) (1990).